High-Spin (*S* = 1) Blatter-Based Diradical with Robust Stability and Electrical Conductivity

Shuyang Zhang[†], **Maren Pink**[#], **Tobias Junghoefer**[§], **Wenchao Zhao**[⊥], **Sheng-Ning Hsu**[⊥], **Suchada Rajca**[†], **Arrigo Calzolari**[^], **Bryan W. Boudouris**[*,⊥,‡], **Maria Benedetta Casu**[*,§], **Andrzej Rajca**[*,†]

[†]Department of Chemistry, University of Nebraska, Lincoln, Nebraska 68588-0304, United States.

[#]IUMSC, Department of Chemistry, Indiana University, Bloomington, Indiana 47405-7102, United States.

[§]Institute of Physical and Theoretical Chemistry, University of Tübingen, 72076 Tübingen, Germany.

[⊥]Charles D. Davidson School of Chemical Engineering, Purdue University, West Lafayette, IN 47907, United States.

[‡]Department of Chemistry, Purdue University, West Lafayette, IN 47907, United States.

[^]CNR-NANO Istituto Nanoscienze, Centro S3, I-41125 Modena, Italy.

Abstract

Triplet ground-state organic molecules are of interest with respect to several emerging technologies but usually show limited stability, especially, as thin films. We report an organic diradical, consisting of two Blatter radicals, that possesses a triplet ground state with a singlet-triplet energy gap, $E_{ST} \approx 0.4 - 0.5$ kcal mol^{-1} ($2J/k \approx 220 - 275$ K). The diradical possesses robust thermal stability, with an onset of decomposition above 264 °C (TGA). In toluene/chloroform, glassy matrix and fluid solution, an equilibrium between two conformations with $E_{ST} \approx 0.4$ kcal mol^{-1} and $E_{ST} \approx -0.7$ kcal mol^{-1} is observed, favoring the triplet ground state over the singlet ground state conformation in the 110 – 330 K temperature range. The diradical with the triplet ground state conformation is found exclusively in crystals and in a polystyrene matrix. Crystalline neutral diradical is a good electrical conductor with conductivity comparable to the thoroughly optimized bis(thiazolyl)-related monoradicals. This is surprising because triplet ground state implies that the underlying π-system is cross-conjugated and thus is not compatible with either good conductance or electron delocalization. The diradical is evaporated under ultra-

[*]Corresponding Authors: arajca1@unl.edu, benedetta.casu@uni-tuebingen.de, boudouris@purdue.edu.

high vacuum to form thin films, which are stable in air for at least 18 h, as demonstrated by X-ray photoelectron and electron paramagnetic resonance (EPR) spectroscopies.

Graphical Abstract
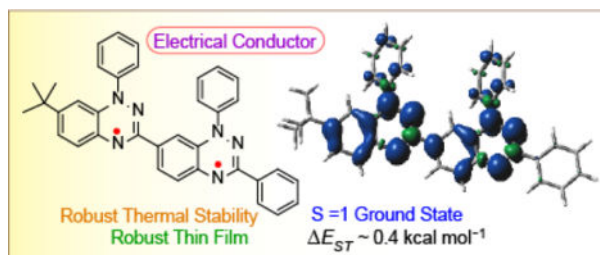
INTRODUCTION

The recently reported high spin organic diradicals **1** and **2** have attracted interest due to their remarkable thermal stability that permits vapor-based growth of thin films under high- or ultra-high vacuum (UHV).[1,2] The design of the diradicals[3,4] is based on the 1,2,4-benzotriazinyl (Blatter) radical substituted with a nitronyl nitroxide (NN) radical, taking advantage of the Blatter monoradical high thermal stability and the NN molecular weights to facilitate film formation. However, **1** and **2** possess limited stability with onset of decomposition <180 °C (thermogravimetric analysis, TGA), and consequently, the diradical thin films, in particular of **2**, undergo rapid decomposition in air.[2,5,6]

We consider a diradical based entirely on the Blatter radical building block, to fully take advantage of its excellent thermal stability.[7–12] The design and synthesis of such diradicals is a huge challenge. There are a few molecules that formally incorporate two Blatter radicals reported to date, e.g., zwitterionic TetraPhenylHexaazaAnthracene (TPHA), *ortho*-DiBlatterTrimethylenemethane (*o*-DBT) or Chichibabin-type diradicaloid **3**.[13–18] These molecules exclusively possess low-spin ($S = 0$) ground states. This is not surprising. According to the Ovchinnikov parity models, TPHA, diradicaloid **3**, and its biphenyl isomers are predicted to possess $S = 0$ ground states, because of the absence of significant spin sign alternation at the atoms connecting two radicals.[19–22] Although the alternating spin connectivity in *o*-DBT predicts the $S = 1$ ground state, severe out-of-plane twisting is well-known to lead to an $S = 0$ ground state.[23] We note that the Blatter triradical based on the classic 1,3,5-phenylene unit was recently reported without experimental evidence for the ground state.[24] This triradical is likely to possess near degenerate high- and low-spin states, similarly to the analogous bis-verdazyl diradical with very small singlet-triplet energy gap, $E_{ST} \approx 0.039$ kcal mol^{-1}.[25,26]

Examination of the parity models and spin density distribution in the parent Blatter radical leads us to a connection at the C3 and C7 position that would provide a high-spin diradical (Figure 1). We design the di-Blatter diradical **4** by taking advantage of the negative spin density at C3 within the Blatter radical moiety (green dot, Figure 1). A *tert*-butyl group at the site of the largest spin density in the annelated benzene ring would enhance stability and solubility of the diradical.[1]

We set out to explore the synthesis of di-Blatter diradical and faced a tremendous challenge with various unsuccessful convergent synthetic approaches. The breakthrough was achieved using a divergent route, in which two benzotriazinyl rings are formed in one synthetic step (Scheme 1).

Here we report the synthesis, characterization and thin-film preparation of di-Blatter diradical **4**. The diradical possesses a triplet ground state and robust thermal stability, with an onset of decomposition above 264 °C – the highest temperature among high-spin diradicals or triradicals studied by TGA.[1,2,27–30]

Remarkably, single crystals of **4** exhibit electrical conductivity, with an outstanding $\sigma \approx 0.04 \pm 0.01$ S cm^{-1} at room temperature, as measured by a two-probe method ($n = 15$ samples). SQUID magnetometry and EPR spectra (and XPS) of polycrystalline **4** also suggest that it is conductive. Typical neutral π-radicals that are insulators have $\sigma < 10^{-10}$ S cm^{-1}, compared to conductive radicals such as the recently reported bis(thiazolyl)-related radicals with $\sigma \approx 0.04$ S cm^{-1},[31] trioxotriangulene radicals with $\sigma \approx 0.002$ S cm^{-1},[32] nitroxide-based glassy polymers with $\sigma \approx 0.3$ S cm^{-1},[33] and bis(phenalenyl) radicals with $\sigma \approx 0.3$ S cm^{-1}.[34] The observation of good electrical conductivity in our high-spin diradical is unusual, because the corresponding π-system is cross-conjugated and thus not conducive to electron delocalization[35–37] or conductance.[38–40] The diradical can be evaporated under UHV to obtain thin films of **4** on silicon substrates, which remain unchanged after exposure to air for at least 18 h.

RESULTS AND DISCUSSION

Synthesis.

The synthesis of **4** starts with the copper-catalyzed C-N bond coupling reaction of **5** with methyl 4-amino-3-iodo-benzoate to produce **6**. The ester group in **6** is hydrolyzed and the resultant carboxylic acid **7** is activated with 1,1'-carbonyldiimidazole (CDI), followed by the reaction with phenylhydrazine. The resultant synthetic intermediate **8** is subjected to a C-N bond coupling reaction with 4-*tert*-butyl-2-iodo-aniline to provide compound **9**. Acid-catalyzed double cyclization of **9** is followed by air oxidation under basic conditions to produce diradical **4** in about 50% isolated yield. Notably, when the cyclization step is carried out for 24 h, instead of 2 h, an approximately equimolar mixture of diradical **4** and by-product monoradical **10** is isolated (Scheme 1). Contraction of paramagnetic 6-membered benzo[e][1,2,4]triazinyl ring to 5-membered benzimidazole ring was observed both in Blatter radicals and in TPHA (Figure 1) (discussion in the SI, p. S26).[41,42]

X-ray crystallography.

Structures of **4** and **10** are confirmed by X-ray crystallography (Figure 2 and SI). In diradical **4**, two fused-ring Blatter radical moieties are nearly coplanar, as indicated by the mean deviation from plane of 0.0719 Å for the plane defined by the N1–N6 and C1–C20 atoms. Also, the dihedral angle along the C4–C5 bond is 8.20 (0.12)°.[43] Thus, the conformation adopted by **4** in the crystal is near optimum for attaining both strong ferromagnetic coupling and electrical conductivity.

Molecules of **4** form one-dimensional (1-D) π-stacks along the crystallographic *a*-axis, which coincides with the longest dimension of the single crystal plate/needle (Figure 2C), with average plane-to-plane distance of 3.482 Å (planes defined by the N1–N6 and C1–C20 atoms). In addition to a short C10···C12 = 3.381 Å contact within the 1-D π-stack, there are multiple C···C and N···C contacts within the sum of van der Waals radii plus 0.1 Å distances (Figs. S1 and S3, SI). Because most of these contacts involve atoms with positive spin densities, relatively strong intermolecular antiferromagnetic interactions are anticipated in crystalline diradical **4**.[2,44]

EPR spectroscopy, SQUID magnetometry, and DFT computations: ground state and conformations of diradical.

EPR spectra of diradical **4** in a frozen glass at 110 K indicate a significant population of the triplet state. The forbidden $|m_s| = 2$ transition is relatively intense, which is consistent with a large spectral width ($2D = 782$ MHz) of the $|m_s| = 1$ region (Figure 3 and Table 1).

D- and *g*-tensor orientations for **1**, **2**, and **4** are similar and the absolute values are well reproduced by DFT-computations[45,46] for two major conformers, **4**A and **4**B, of **4**, except for the inherently difficult to compute parameter *E*.

DFT computations at the UB3LYP/6–31G(d,p)+ZPVE level, reveal that conformer **4**A, corresponding to that found in crystalline **4** (Figure 2), is a global minimum with energy preference for triplet states from 0.05 (gas phase) to 0.14 (tetrahydrofuran, THF) kcal mol^{-1}, compared to **4**B (Table 2). We compute $E_{ST} \approx 1.37$ kcal mol^{-1} for **4**A that is considerably greater than $E_{ST} \approx 0.34$ kcal mol^{-1} for **4**B. Analogously in THF, we obtain, $E_{ST} \approx 1.22$ and 0.22 kcal mol^{-1} for **4**A and **4**B, respectively. Because the $E_{ST} > 0$ is oversestimated at this level of theory,[47–49] conformer **4**B may actually be a singlet ground state, i.e., with $E_{ST} < 0$.

In addition, intermolecular $J'/k \approx -100$ K is computed for the π-dimer using the X-ray geometry (Table S14, SI). This supports anticipated strong antiferromagnetic interactions in crystalline **4**, as inferred from X-ray crystal packing, likely leading to electrical conductivity.

We employ EPR spectroscopy to determine the triplet ground state of **4** in toluene/chloroform (4:1) and in a polystyrene matrix by measurement of χT, the product of paramagnetic susceptibility (χ) and temperature (*T*), in the $T = 110 - 331$ K and $T = 110 - 341$ K range, respectively (Figure 4).[1,25,50] The spectra are acquired at each *T* at least in triplicate. Tempone in toluene/chloroform (4:1) and DPPH in polystyrene are used as spin counting references.

The sample of **4** in the polystyrene matrix is prepared by dissolving **4** and polystyrene in THF, to favor conformer **4**A (Table 2), and then the solvent is evaporated under vacuum, to essentially "lock" conformer **4**A in polystyrene, which possesses a relatively high glass transition temperature, $T_g \approx 373$ K, and forms a relatively rigid glass.[51,52] In contrast, we anticipate that the toluene/chloroform (4:1) solution/matrix will allow for equilibration of the two conformers **4**A and **4**B; e.g., pure toluene glass has a relatively low $T_g = 117$ K and even below T_g exhibits pronounced secondary relaxation.[51,52]

For **4** in toluene/chloroform (4:1), the numerical fit of χT vs. T to the modified Bleaney-Bowers-like equation (eq. S2, SI)[2,36,50] suggests the presence of two equilibrating conformations **4A** and **4B** with singlet-triplet energy gaps $2J_A/k = 220 \pm 70$ K and $2J_B/k = -340 \pm 37$ K, i.e., $E_{ST} \approx 0.4$ kcal mol^{-1} for the major conformation **4A** (Figure 4A). Also, this fit suggests that the ratio of **4A**/**4B** is about 2:1 and 1:1 at 331 and 110 K, respectively. For **4** in the polystyrene matrix, χT vs. T dependence is qualitatively different and corresponds to one major conformer with a triplet ground state and singlet-triplet energy gap $2J/k = 275 \pm 36$ K, i.e., $E_{ST} \approx 0.5$ kcal mol^{-1} (Figure 4B).

Finally, another more concentrated 41 mM sample of **4** in polystyrene was used to obtain SQUID magnetization data (Fig. S14, SI). Because the M/M_{sat} vs H/T data at $T = 1.8, 3,$ and 5 K approximately coincide with the $S = 1$ Brillouin curve, this provides unequivocal evidence for the triplet ground state of diradical **4**.

Electrical Conductivity and Magnetic Characterization of 4 in the Solid State.

Single crystal conductivity, σ, measurements are carried out along needle axis in the 320 – 9 K range. As noted in the X-ray crystallography sub-section (Figure 2C), the needle axis coincides with direction of 1-D π-stacks along the crystallographic a-axis. For the 15 randomly selected single crystals, values of σ at room temperature ranged from 0.003 to 0.13 S cm^{-1}, giving $\sigma = 0.044 \pm 0.012$ S cm^{-1} (mean $\pm$ SE). Measurements on spin-coated films give much lower $\sigma = {\sim}1 \times 10^{-4}$ S cm^{-1}, SI. Notably, for all studied single crystal samples, the σ vs T dependence follows an approximately linear relationship with statistically adjusted correlation coefficient, adj $R^2 = 0.930 - 0.996$ (Figure 5A, inset plot, Tables S8 and S9, SI). This unusual linear relationship corresponds to temperature-dependent activation energy, E_a/k.[53] As illustrated in Figure 5A (main plot), activation energies are: $E_a/k \approx 140$ K (~12 meV) in the high temperature range ($T = 200 - 320$ K) and $E_a/k \approx 0.4$ K (~0.03 meV) in the low temperature range ($T = 9 - 20$ K). This nearly temperature-independent behavior (i.e., $E_a/k << T$) is indicative of band-like transport. For comparison, single crystals of bis(thiazolyl) and bis(phenalenyl) monoradicals, with optimized structures for electrical conductivity, exhibited much larger $E_a = 50$ and 54 meV, respectively.[31,34] While not common in organic electronics, this behavior has been observed in other radical systems,[33] and it has been seen with respect to charge transport in well-studied single crystal rubrene systems,[54,55] single crystal pentacene systems,[56] and thin film pentacene systems[57] when trap sites were minimized. Due to the high quality of the single crystals and our ability to measure conductivity along the preferred transport direction, similar conclusions can be reached here. That is, the weak temperature dependence is likely due to transport that is approaching that of band-like behavior, and this is accentuated at lower temperatures as carrier-phonon interactions are lowered.

This "near-metal-like" behavior is confirmed by magnetic studies of polycrystalline diradical **4**. The static paramagnetic susceptibility (χ) is nearly temperature independent in the range from 20 to 320 K, and the value of $\chi \approx 2 - 3 \times 10^{-3}$ emu mol^{-1} is consistent with Pauli paramagnetism (Figure 5B). This value of χ is significantly greater than $\chi \approx 5 - 6 \times 10^{-4}$ emu mol^{-1} observed in bis(phenalenyl) and bis(thiazolyl) monoradicals.[31,34] However, it is smaller than $\chi \approx 4 - 12 \times 10^{-3}$ emu mol^{-1} determined by Dunbar and coworkers for

"planarized" oligomers of heavily p-doped polyaniline.[58] In addition, we note the residual paramagnetism from some crystals in the polycrystalline sample, appears as a shallow broad maximum at about 200 K, due to one-dimensional $S = 1$ antiferromagnetic chains with a large $J/k \sim -150$ K.[2,44,59] The Curie behavior, χ vs $1/T$, observed below 20 K corresponds to the presence of residual paramagnetic centers (defects) at a concentration of 2.5 – 3% in the crystal lattice.

The EPR spectroscopy on polycrystalline **4**, with particle sizes <75 μm, confirms the temperature independent χ in the $T = 110 – 331$ K range (Figure 5C); EPR spectra possess Dysonian lineshape ($A/B > 1$), characteristic of a conducting solid (Figure 5D).[60–62]

Electrochemistry and UV-vis-NIR spectroscopy.

Voltammetry (cyclic, differential pulse, and square wave) for diradical **4** shows reversible oxidation of Blatter radical moieties at $E^{+/0} \approx +0.18$ V and $E^{2+/+} \approx +0.42$ V, vs SCE (Figure 6). At the same conditions, reduction of **4** at $E^{-/0} \approx -0.87$ V and $E^{2-/-} \approx -1.14$ V (DPV) is progressively more irreversible as indicated by shapes of cyclic voltammogram and peak broadening in the differential pulse voltammetry. These values may be compared to $E^{+/0} \approx +0.4$ V, associated with the oxidation of Blatter radical moieties in the high-spin diradical **2** as well as related triradical, determined under identical conditions.[25] Also, for a typical planarized Blatter radical in dichloromethane, $E^{+/0} = +0.31$ V and $E^{-/0} = -0.86$ V (vs. SCE) redox potentials were reported.[63]

UV-vis-NIR absorption spectra of diradical **4** in dichloromethane consist of four major bands at 303, 384, 520, and 720 nm (Figure 7). Diradical **4** has an absorption onset in the 1181–1216 nm range, corresponding to an optical gap, $E_g = 1.04 \pm 0.01$ eV. This value is much smaller than $E_g = 1.42 \pm 0.01$ eV for diradical **2** and the corresponding triradical,[25] as well as $E_g = 1.6 – 1.7$ eV for "planarized" Blatter monoradicals.[63,64] The UV-vis-NIR spectrum for diradical **4** is reproduced by the TD-DFT computations at the UCAM-B3LYP/6–31+G(d,p)/IEF-PCM-UFF level of theory employing a dichloromethane solvent model (Fig. S58, SI).

We confirm that the long wavelength band at $\lambda = 720$ nm (with shoulder at 950 nm) originates from diradical **4** and not from its partially oxidized form. We carry out oxidation of **4** to its radical cation with one-electron oxidant [Cp$_2$Fe][BF$_4$] (1.2 equiv). UV-vis-NIR absorption spectra for the radical cation in DCM indicate that the band at $\lambda = 720$ nm (and its long-wavelength shoulder) is diminished while a new, much more intense, band at $\lambda \approx 1540$ nm ($\varepsilon \approx 2 \times 10^3$ L mol^{-1} cm^{-1}) appears. EPR spectra for the radical cation in n-butyronitrile glass at 117 K are characteristic of an $S = \frac{1}{2}$ radical (Figs. S10 and S11, SI). In contrast to diradical **4**, for the radical cation, conformation **4B**$^{\cdot+}$ is by far dominant in DCM solution based on DFT computations (Table S15, SI), as confirmed by a good fit of the TD-DFT computed spectra to the experimental UV-vis-NIR absorption spectra (Fig. S59, SI).

In summary, diradical **4** in dichloromethane at room temperature has an optical and electrochemical gap, $E_g \approx 1$ eV and it is anticipated, based on EPR spectroscopic studies in toluene/chloroform that the diradical will exist as a ~2:1 mixture of conformations **4A**

and **4**B with triplet and singlet ground states, respectively. Conformations **4**A and **4**B are expected to possess nearly identical redox potentials, and TD-DFT studies suggests the same for their absorption spectra.

DFT studies of band structure for crystalline 4.

The intermolecular coupling is investigated through the electronic structure investigation of crystalline **4** in the solid state. The simulation cell includes molecules stacked along the *a*-axis (see: SI), whose initial coordinates stem from the X-ray crystallography studies described above. The ground state corresponds to an antiferromagnetic phase, with an average magnetic moment $\mu = 2.7$ Bohr magnetons per molecule, in agreement with the experimentally determined triplet ground state for molecule of **4**.

Band structure and density-of-states (DOS) for crystalline **4** at the B3LYP level of theory[65,66] are characteristic of a pure large bandgap semiconductor (Figure 8), with no defect states in the gap.

The computations reveal some features that lead to increased conductivity, such as near degenerate pairs of singly occupied (S_O) and singly unoccupied (S_U) bands which derive from the π-coupling of the corresponding molecular orbitals (see Fig. S60, SI). The S_O and S_U bands have an energy dispersion of ca. 150 meV within each pair, especially along the $\Gamma \rightarrow Y$ direction, corresponding to π-stacked molecules along the crystallographic *a*-axis. Since $S_{O1,2}$ and $S_{U1,2}$ states are close in energy and overlap in space, thermal broadening may easily couple the single S_O and S_U bands to form manifolds of π-π extended states, whose effective dispersion is ~240 meV and 250 meV, for S_O and S_U, respectively (see: DOS in Figure 8), which act as conductive π-channel for electron transport (Fig. S61, SI). This justifies the high conductivity and the temperature dependence observed in the experiments. This is confirmed by the simulation of the Boltzman conductivity, which reveals preferential conductivity by ca. two orders of magnitude along crystallographic *a*-axis vs. *b*- or *c*-axes (Fig. S62, SI).

However, our computational results on pure crystalline **4** are not compatible with near-metal-like conductivity with very low activation barrier. Thus, it is reasonable to suspect that free carriers are introduced to the experimental system (e.g., surface site defects and/or band bending at the metal-organic interface) that are not captured well in simulations associated with the single crystal structure. In fact, a similar phenomenon has been observed experimentally in a related radical system. That is, Venkataraman and co-workers previously demonstrated that, while the substituted Blatter monoradical is stable on a gold substrate under ultrahigh vacuum, the solution-based single-molecule conductance measurements at 0.2 V, indicate that the radical is oxidized to the closed-shell cation as a result of charge transfer occurring from the molecule to the gold electrodes.[67] Therefore, we computed DOS for crystalline **4** with its unit cell ($N = 4$ molecules) possessing +1 charge ($Q = +1$), i.e., including a hole in the system. The computations reveal that the removal of the electron did not change dramatically the band structure of the neutral system ($Q = 0$), except for the S_O manifold, with the hole (positive charge) delocalized within the entire unit cell (i.e., no polaron formation). Nonetheless, this breaks the degeneracy between the S_{O1} and S_{O2} peaks, with the latter peak (labeled A in Figure 8) remaining partially occupied. This causes

the pinning of the Fermi level on the top of the valence band. The combination of both neutral and partially charged contributions result in a typical picture of a p-type doped semiconductor, where the A state, which is shifted in energy by ~0.12 eV with respect to the valence band top of the neutral system, acts as electron-acceptor state. The appearance of the defect state A is in agreement with the low $E^{+/0}$ redox potential observed in the voltammetric experiments and the conducting character (i.e., low activation energy) resulting from the transport measurements.

Thermal stability and thin films.

TGA, with parallel IR spectroscopy, of diradical **4** indicates that the onset of decomposition is at $T > 264$ °C, which is more than ~100 °C higher than recently studied $S = 1$ diradical **2** (Figure 9).[2] Relying on this result, we deposit thin films of diradical **4** on SiO_2/Si(111) wafers by controlled evaporation under ultra-high vacuum (UHV). Following a well-established method,[5,11,68] we use X-ray photoelectron spectroscopy (XPS) together with a best fit procedure to assess the intactness of the diradical in the thin films and the film lifetime under air exposure.[69] The XPS investigations indicate that the films have the expected stoichiometry (Figure 9), i.e., the evaporation of intact radicals was successfully achieved. This is further supported by the direct comparison with the XPS spectra of the powder, that did not undergo evaporation, and EPR spectroscopy (SI).

The XPS signal attenuation upon film deposition (Figure 10, top panel) is characterised by a very slow decay. This intensity trend hints at a Volmer-Weber (VW) growth mode, i.e., island growth. This result is consistent with the *ex-situ* AFM images obtained on diradical **4** films (Figure 10, bottom panel) clearly showing a film morphology dominated by islands, indicating that the interaction between molecules is much stronger than the interaction with the substrate (Figure 10).

Comparing the XPS spectra of the films and those of the powder, we note that their similarity is remarkable (Figure 9). Usually, the XPS lines of the powder are characterised by a larger bandwidth when compared to the spectra of the films because of charging effects.[70] Analysing the broadening of the powder C 1s line, we see that it is 0.08 eV larger than that of the film. This is a very small value in comparison with other radicals. In fact, we have previously investigated a derivative of the Blatter radical that shows a similar, although slightly larger, difference (0.09 eV).[10] In contrast, in the spectra of nitronyl nitroxide radical derivatives, including diradical **2** and related triradical this difference is large (0.50 eV).[2,5,25,68] This observation supports the result that polycrystalline diradical **4** is a good electrical conductor, being able to screen the core-hole created upon photoemission more efficiently than nitronyl nitroxide radical derivatives[2,5,25,68] and various closed-shell systems.[70]

We have also monitored the lifetime of the films exposed to air at room temperature (see the supporting information, Figure S48). We have found that the films exposed to air do not show any changes in the N 1s core level spectra for at least 18 hours. This can be considered a long film lifetime in comparison with other diradical and triradical thin films. In our previous work,[5] we have found that stability of the film under ambient air depends on the delocalization of the unpaired electrons and the onset of decomposition in TGA. The

larger the delocalization and the higher the onset, the more stable are the films exposed to air. The results obtained for diradical **4** thin films fully confirm this correlation. In fact, they show the longest lifetime for polyradical thin films that was measured so far, presumably because of the significant delocalization of the unpaired electrons (Table 2).

CONCLUSION

We have prepared the first high-spin ($S = 1$) diradical, based entirely on two Blatter radical moieties, to attain robust thermal stability. The single crystals of diradical **4** display good electrical conductivity, observed for the first time in a high-spin diradical. Remarkably at low temperatures, activation energies for conductivity become negligible (<1 K or <0.1 meV), thus the material approaches metal-like behavior. Electrical conductivity of polycrystalline **4** is also supported by SQUID magnetometry, EPR spectroscopy, and XPS spectra. DFT band structure studies of crystalline **4** show the formation of effective manifolds of near-degenerate pairs of singly occupied (SO) and singly unoccupied (SU) bands, each with dispersion of ca. 250 meV, which act as π-like "conducting channel" in crystalline **4**. The presence of hole states in the system imparts a p-doped character to the sample, which behave an intrinsic degenerate semiconductor. The diradical is evaporated under UHV to form thin films on silicon, which are relatively stable under vacuum (many days) or under air (at least 18 h).

We are working on the synthesis of $S = 3/2$ Blatter-based triradical, homologue of **4**. Will it provide even better electrical conductor, due to triply near-degenerate SO and SU bands?

EXPERIMENTAL SECTION

X-ray Crystallography.

A small, black crystal of **4** was placed on a Bruker Venture D8 diffractometer equipped with a Cu-IμS Diamond source (Incoatec) and a PhotonIII detector. Data were collected at 100 K. Crystal data for **4**: black needle, $0.058 \times 0.012 \times 0.008$ mm^3, $C_{36}H_{30}N_6$, $M =$ 546.66, monoclinic, P2$_1$/c, $a = 5.6659(4)$ Å, $b = 20.7381(12)$ Å, $c = 22.9577(15)$ Å, $\beta =$ 102.668(2)°, $V = 2685.6(3)$ Å^3, $Z = 4$, $\rho_{calcd} = 1.469$ Mg/m^3, $\mu = 0.627$ mm^{-1}, CuKα radiation ($\lambda = 1.54178$ Å). A total of 34729 reflections were measured of which 4797 ($R_{int} = 0.2092$) were independent and 2135 observed [$I > 2\sigma(I)$]. Data were corrected for absorption.[71] The structure was solved with direct-methods[72] and refined with full-matrix least squares / difference Fourier cycles.[73] All non-hydrogen atoms were refined with anisotropic displacement parameters. The hydrogen atoms were placed in ideal positions and refined as riding atoms with relative isotropic displacement parameters. The final anisotropic full-matrix least-squares refinement on F^2 with 382 variables converged at R1 = 7.91%, for the observed data and wR2 = 27.63% for all data. The goodness-of-fit was 0.960 and the largest peak and hole in the final difference electron density synthesis were 0.285 e$^-$/Å^3 and −0.265 e$^-$/Å^3, respectively, with an RMS deviation of 0.062 e$^-$/Å^3. A Bravais Friedel Donnay Harker (BFDH) calculation,[74–76] predicting the growth morphology of crystals based on crystallographic geometrical consideration and as implemented in MERCURY,[77] was performed and corresponds to the observed, indexed crystal morphology,

confirming that the needle direction and the stacking direction of the molecule is along the crystallographic *a*-axis.

Further details, including the data acquisition and refinement, are described in the Supporting Information and the CIF files, deposited with the CCDC.

Synthesis of 4.

Standard techniques for synthesis under inert atmosphere (argon or nitrogen), using custom-made Schlenk glassware, custom-made double manifold high vacuum lines, argon-filled MBraun glovebox, and nitrogen- or argon-filled glovebags were employed. Chromatographic separations were carried out using normal phase silica gel. Syntheses of the intermediates **5 – 9** and monoradical **10** are described in the SI.

Optimized procedure for diradical 4.—To the starting material **9** (40 mg, 68.5 μmol), and *p*-TsOH•H$_2$O (26 mg, 137 μmol), toluene (14 mL) was added. The stirred reaction mixture was refluxed with the custom-made micro-scale Dean-Stark apparatus[44] in the dark for 2 h. The resultant reaction mixture became a black solution. Then, after evaporation of the solvent, the dark green-black residue was dissolved in EtOH/ 2M NaOH, 1:1 (60 mL) to provide a dark brown-red solution. The reaction mixture was stirred under air for 4 h, and then extracted with DCM (20 mL × 3). After the removal of the solvent, the TLC analysis showed diradical **4** as the major spot with $R_f = 0.2$ (neutral alumina, DCM/pentane, 10:4). After column chromatography, the isolated yield was 19.6 mg (52%) with spin concentration of about 200% at room temperature. The diradical **4** could be recrystallized by the vapor diffusion method with ethyl acetate and pentane to increase purity (SI).

Magnetic characterization of 4: EPR spectroscopy and SQUID magnetometry.

EPR spectra were obtained on a CW X-band spectrometer (Bruker, EMX-plus) and were simulated using EasySpin.[78] SQUID magnetometry data were acquired using 5-Tesla Quantum Design SQUID magnetometer with the samples contained in colorless gelatin capsules (polycrystalline solid) or in custom-made EPR quartz tubes (polystyrene matrix).[2,25,79] Samples of **4** contained less than 3.6% of diamagnetic impurities (Fig. S15, SI).

UV-vis-NIR absorption spectroscopy and electrochemistry.

UV-vis-NIR absorption spectra were acquired on a JASCO-V-670 spectrophotometer in DCM; the spectral range was $\lambda = 250 – 1800$ nm for **4** and $\lambda = 250 – 2500$ nm for the oxidation of **4** to its radical cation. Voltammetry (cyclic, square wave, and differential pulse) data were obtained using a VersaSTAT 4 potentiostat/galvanostat and 0.1 M tetrabutylammonium hexafluorophosphate supporting electrolyte in DCM. Decamethyl ferrocene was employed as a potential reference (–0.130 V vs. SCE for Cp*$_2$Fe/Cp*$_2$Fe$^+$ in DCM),[80] in conjunction with Ag-wire pseudo-reference electrode.

Solid State Electrical Conductivity Measurements.

For both single crystals and thin films of the radical species **4**, electrical conductivity measurements were made using a two-point contact geometry (see: SI for the fabrication

procedures) with all conductivity measurements performed while the samples were housed in a vacuum probe station. The temperature-dependent measurements were made as a function of cooling (and warming) from approximately room temperature to near liquid-helium temperatures. For each measurement, the sample was allowed to reach a thermal steady-state with the temperature stage prior to acquisition of the current response as a function of voltage. These *I-V* traces were used to extract the resistance, and ultimately the conductivity (see: SI), of the single crystal and thin film samples. At temperatures < 50 K, slightly non-ohmic behavior was observed in the *I-V* traces, and this is likely due to interfacial effects that arise at these temperatures.

Electronic Band Structure Calculations.

Solid state calculation on crystalline **4** were carried out with the QUANTUM ESPRESSO.[81] Perdew–Burke–Ernzerhof (PBE) functional[65] was used to the optimize the atomic structure of the system. The electronic structure was evaluated at the B3LYP level,[66,82] without further atomic relaxation. Atomic potentials were described by ultra-soft pseudopotentials, while single particle wavefunctions (charge) were expressed in planewave with a cut-off energy of 30 Ry (300 Ry), respectively. Starting coordinates for geometry optimizations were taken from the single crystal structure of **4**. A $(2 \times 2 \times 2)$ Monkhorst–Pack sampling scheme was used for Brillouin zone integration during the relaxation step, Γ-only was used for the electronic structure calculation. Electron transport properties have been evaluated by solving the Boltzmann semiclassical equation, within the scattering time approximation,[83] by using PAOFLOW code.[84] More details in the SI.

Thin Films of 4.

Thin films were prepared in situ under UHV conditions by organic molecular beam deposition (OMBD) using a calibrated Knudsen cell. Native SiO_2 grown on single-side polished n-Si(111) wafers were used as a substrate. The XPS spectra were measured using a monochromatic Al Kα source and a SPECS Phoibos 150 hemispherical electron analyser. Atomic force microscopy was measured under ambient conditions with a Digital Instrument Nanoscope III Multimode microscope using tapping mode. Further details are given in SI.

Supplementary Material

Refer to Web version on PubMed Central for supplementary material.

ACKNOWLEDGMENT

REFERENCES

(1). Gallagher NM; Bauer JJ; Pink M; Rajca S; Rajca A High-Spin Organic Diradical with Robust Stability. J. Am. Chem. Soc 2016, 138, 9377–9380. [PubMed: 27430499]

(2). Gallagher N; Zhang H; Junghoefer T; Giangrisostomi E; Ovsyannikov R; Pink M; Rajca S; Casu MB; Rajca A Thermally and Magnetically Robust Triplet Ground State Diradical. J. Am. Chem. Soc 2019, 141, 4764–4774. [PubMed: 30816035]

(3). Abe M Diradicals. Chem. Rev 2013, 113, 7011–7088. [PubMed: 23883325]

(4). Ratera I; Veciana J Playing with organic radicals as building blocks for functional molecular materials. Chem. Soc. Rev 2012, 41, 303–349. [PubMed: 21850355]

(5). Junghoefer T; Gallagher N; Kolanji K; Giangrisostomi E; Ovsyannikov R; Chassé T; Baumgarten M; Rajca A; Calzolari A; Casu MB Challenges in controlled thermal deposition of organic diradicals. Chem. Mater 2021, 33, 2019–2028.

(6). Calzolari A; Rajca A; Casu MB From radical to triradical thin film processes: the Blatter radical derivatives. J. Mater. Chem. C, 2021, 9, 10787–10793.

(7). Blatter HM; Lukaszewski H A new stable free radical. Tetrahedron Lett. 1968, 9, 22, 2701–2705.

(8). Constantinides CP; Koutentis PA; Krassos H; Rawson JM; Tasiopoulos AJ Characterization and Magnetic Properties of a "Super Stable" Radical 1,3-Diphenyl-7-trifluoromethyl-1,4-dihydro-1,2,4-benzotriazin-4-yl. J. Org. Chem 2011, 76, 2798–2806. [PubMed: 21384906]

(9). Zheng Y; Miao M-S; Kemei MC; Seshadri R; Wudl F The Pyreno-Triazinyl Radical – Magnetic and Sensor Properties. Isr. J. Chem 2014, 54, 774–778.

(10). Ciccullo F; Gallagher NM; Geladari O; Chasse T; Rajca A; Casu MD A Derivative of the Blatter Radical as a Potential Metal-Free Magnet for Stable Thin Films and Interfaces. ACS Appl. Mater. Interfaces 2016, 8, 1805–1812. [PubMed: 26727145]

(11). Casu MB, Nanoscale studies of organic radicals: surface, interface, and spinterface. Acc. Chem. Res 2018, 51, 753–760. [PubMed: 29465979]

(12). Rogers FJM; Norcott PL; Coote ML Recent advances in the chemistry of benzo[e][1,2,4]triazinyl radicals. Org. Biomol. Chem 2020, 18, 8255–8277. [PubMed: 33001120]

(13). Hutchison K; Srdanov G; Hicks R; Yu H; Wudl F Tetraphenylhexaazaanthracene: A Case for Dominance of Cyanine Ion Stabilization Overwhelming 16π Antiaromaticity. J. Am. Chem. Soc 1998, 120, 2989–2990.

(14). Constantinides CP; Zissimou GA; Berezin AA; Ioannou TA; Manoli M; Tsokkou D; Theodorou E; Hayes SC; Koutentis PA Tetraphenylhexaazaanthracenes: 16π Weakly Antiaromatic Species with Singlet Ground States. Org. Lett 2015, 17, 4026–4029. [PubMed: 26244376]

(15). Zheng Y; Miao M; Dantelle G; Eisenmenger ND; Wu G; Yavuz I; Chabinyc ML; Houk KN; Wudl F A Solid-State Effect Responsible for an Organic Quintet State at Room Temperature and Ambient Pressure. Adv. Mater 2015, 27, 1718–1723. [PubMed: 25619560]

(16). Hu X; Zhao L; Chen H; Ding Y Zheng Y-Z; Miao M; Zheng Y Air stable high-spin blatter diradicals: non-Kekulé *versus* Kekulé structures. J. Mater. Chem. C 2019, 7, 6559–6563.

(17). Hu X; Chen H; Zhao L; Miao M; Han J; Wang J; Guo J; Hu Y; Zheng Y Nitrogen analogues of Chichibabin's and Müller's hydrocarbons with small singlet–triplet energy gaps. Chem. Commun 2019, 55, 7812–7815.

(18). Hu X; Chen H; Xue G; Zheng Y Correlation between the strength of conjugation and spin–spin interactions in stable diradicaloids. J. Mater. Chem. C 2020, 8, 10749–10754.

(19). Ovchinnikov AA Multiplicity of the ground state of large alternant organic molecules with conjugated bonds. Theor. Chim. Acta 1978, 47, 297–304.

(20). Gallagher NM; Olankitwanit A; Rajca A High-Spin Organic Molecules. J. Org. Chem 2015, 80, 1291–1298. [PubMed: 25574756]

(21). Rajca A; Rajca S Intramolecular Antiferromagnetic vs Ferromagnetic Spin Coupling Through the Biphenyl Unit. J. Am. Chem. Soc 1996, 118, 8121–8126.

(22). Rajca A, Wongsriratanakul J, Rajca S, High-Spin S Organic Polyradicals as Spin Clusters: Ferromagnetic Spin Coupling through Biphenyl Unit in Polyarylmethyl Tri-, Penta-, Hepta-, and Hexadecaradicals. J. Am. Chem. Soc 1997, 119, 11674–11686.

(23). Shultz DA; Fico RM Jr.; Lee H; Kampf JW; Kirschbaum K; Pinkerton AA; Boyle PD Mechanisms of Exchange Modulation in Trimethylenemethane-type Biradicals: The Roles of Conformation and Spin Density. J. Am. Chem. Soc 2003, 125, 15426–15432. [PubMed: 14664588]

(24). Zissimou GA; Berezin AA; Manoli M; Nicolaides C; Trypiniotis T; Koutentis PA 3,3′,3′′-(Benzene-1,3,5-triyl)tris(1-phenyl-1H-benzo[e][1,2,4]triazin-4-yl): A C_3 symmetrical Blatter-type triradical. Tetrahedron 2020, 76, 131077, DOI: 10.1016/j.tet.2020.131077.

(25). Shu C; Pink M; Junghoefer T; Nadler E; Rajca S; Casu MB; Rajca A Synthesis and Thin Films of Thermally Robust Quartet ($S = 3/2$) Ground State Triradical. J. Am. Chem. Soc 2021, 143, 5508–5518. [PubMed: 33787241]

(26). Gilroy JB; McKinnon SDJ; Kennepohl P; Zsombor MS; Ferguson MJ; Thompson LK; Hicks RG Probing Electronic Communication in Stable Benzene-Bridged Verdazyl Diradicals. J. Org. Chem 2007, 72, 8062–8069. [PubMed: 17887707]

(27). Suzuki S; Furui T; Kuratsu M; Kozaki M; Shiomi D; Sato K; Takui T; Okada K Nitroxide-substituted nitronyl nitroxide and iminonitroxide. J. Am. Chem. Soc 2010, 132, 15908–15910. [PubMed: 20964296]

(28). Wang W; Chen C; Shu C; Rajca S; Wang X; Rajca A $S = 1$ Tetraazacyclophane Diradical Dication with Robust Stability: a Case of Low Temperature One-Dimensional Antiferromagnetic Chain. J. Am. Chem. Soc 2018, 140, 7820–7826. [PubMed: 29863339]

(29). Tretyakov EV; Zhivetyeva SI; Petunin PV; Gorbunov DE; Gritsan NP; Bagryanskaya IY; Bogomyakov AS; Postnikov PS; Kazantsev MS; Trusova ME; Shundrina IK; Zaytseva EV; Parkhomenko DA; Bagryanskaya EG; Ovcharenko VI Ferromagnetically Coupled $S = 1$ Chains in Crystals of Verdazyl-Nitronyl Nitroxide Diradicals. Angew. Chem. Int. Ed 2020, 59, 20704–20710.

(30). Tretyakov EV; Petunin PV; Zhivetyeva SI; Gorbunov DE; Gritsan NP; Fedin MV; Stass DV; Samoilova RI; Bagryanskaya IY; Shundrina IK; Bogomyakov AS; Kazantsev MS; Postnikov PS; Trusova ME; Ovcharenko VI Platform for High-Spin Molecules: A Verdazyl-Nitronyl Nitroxide Triradical with Quartet Ground State. J. Am. Chem. Soc 2021, 143, 8164–8176. [PubMed: 34019759]

(31). Mailman A; Wong JWL; Winter SM; Claridge RCM; Robertson CM; Assoud A; Yong W; Steven E; Dube PA; Tse JS; Desgreniers S; Secco RA; Oakley RT Fine tuning the performance of multiorbital radical conductors by substituent effects. J. Am. Chem. Soc 2017, 139, 1625–1635. [PubMed: 28117984]

(32). Murata T; Yamada C; Furukawa K; Morita Y Mixed valence salts based on carbon-centered neutral radical crystals. Nature Comm. Chem 2018, 1, article no. 47.

(33). Joo Y; Agarkar V; Sung SH; Savoie BM; Boudouris BW A nonconjugated radical polymer glass with high electrical conductivity. Science 2018, 359, 1391–1395. [PubMed: 29567710]

(34). Pal SK; Itkis ME; Tham FS; Reed RW; Oakley RT; Haddon RC Resonating valence-bond ground state in a phenalenyl-based neutral radical conductor. Science 2005, 309, 281–284. [PubMed: 16002614]

(35). Utamapanya S; Rajca A Topological Control of Electron Localization in π-Conjugated Polyarylmethyl Carbopolyanions and Radical Anions. J. Am. Chem. Soc 1991, 113, 9242–9251.

(36). Rajca A Organic diradicals and polyradicals: from spin coupling to magnetism? Chem. Rev 1994, 94, 871–893.

(37). Rajca S; Rajca A Novel High-Spin Molecules: π-Conjugated Polyradical Polyanions. Ferromagnetic Spin Coupling and Electron Localization. J. Am. Chem. Soc 1995, 117, 9172–9179.

(38). Tsuji Y; Hoffmann R; Strange M; Solomon GC Close relation between quantum interference in molecular conductance and diradical existence. Proc. Natl. Acad. Sci. U. S. A 2016, 113, E413–E419. [PubMed: 26755578]

(39). Baghernejad M; Zhao X; Baruël Ørnsø K; Füeg M; Moreno-García P; Rudnev AV; Kaliginedi V; Vesztergom S; Huang C; Hong W Broekmann P; Wandlowski T Thygesen KS; Bryce MR Electrochemical Control of Single-Molecule Conductance by Fermi-Level Tuning and Conjugation Switching. J. Am. Chem. Soc 2014, 136, 17922–17925. [PubMed: 25494539]

(40). Mayor M; Weber HB; Reichert J; Elbing M; von Hänisch C; Beckmann D; Fischer M Electric Current through a Molecular Rod—Relevance of the Position of the Anchor Groups. Angew. Chem. Int. Ed. 2003, 42, 5834–5838.

(41). Barton DHR; Ducker JW; Lord WA; Magnus PD Some reactions of thiohydrazides and related compounds. J. Chem. Soc., Perkin Trans 1, 1976, 38–42.

(42). Berezin AA; Koutentis PA Ring contraction of 1,3-diphenylbenzo[1,2,4]triazinyl radicals to 1,2-diphenylbenzimidazoles. Org. Biomol. Chem 2014, 12, 1641–1648. [PubMed: 24477224]

(43). The dihedral angle is between the C1-N1-N2-C2-C3-C4-C12-C13-C14-N6 and C5-N3-N4-C6-C7-C8-C8-C9-C10-C11-N5 planes.

(44). Rajca A; Takahashi M; Pink M; Spagnol G; Rajca S Conformationally constrained, stable, triplet ground state ($S = 1$) nitroxide diradicals: antiferromagnetic chains of ($S = 1$) diradicals. J. Am. Chem. Soc 2007, 129, 10159–10170. [PubMed: 17655296]

(45). Frisch MJ; et al., Gaussian 16, Revision A.1 (Gaussian, Inc., Wallingford CT, 2016).

(46). Neese F The ORCA program system. Wiley Interdisciplinary Reviews: Comp. Mol. Sci 2012, 2, 73–78.

(47). Quast H; Nüdling W; Klemm G; Kirschfeld A; Neuhaus P; Sander W; Hrovat DA; Borden WT A Perimidine-Derived Non-Kekulé Triplet Diradical J. Org. Chem 2008, 73, 4956–4961. [PubMed: 18547111]

(48). Trinquier G; Suaud N; Malrieu J-P Theoretical Design of High-Spin Polycyclic Hydrocarbons. Chem.–Eur. J 2010, 16, 8762–8772. [PubMed: 20572170]

(49). Mañeru DR; Pal AK; Moreira IPR; Datta SN; Illas FJ The Triplet–Singlet Gap in the m-Xylylene Radical: A Not So Simple One. Chem. Theory Comput 2014, 10, 335–345.

(50). Shu C; Zhang H; Olankitwanit A; Rajca S; Rajca A High-Spin Diradical Dication of Chiral π-Conjugated Double Helical Molecule. J. Am. Chem. Soc 2019, 141, 17287–17294. [PubMed: 31596077]

(51). Vogel M; Tschirwitz, Schneider G; Koplin C; Medick P; Rössler E A ^{2}H NMR and dielelectric spectroscopy study of the slow β-process in organic glass formers. J. Non-Crystal. Solids 2002, 307–310, 326–335.

(52). Vogel M; Rössler E Slow β process in simple organic glass formers studied by one- and two-dimensional ^{2}H nuclear magnetic resonance. J. Chem. Phys 2001, 114, 5802–5815.

(53). Worfolk BJ; Andrews SC; Park S; Reinspach J; Liu N; Toney MF; Mannsfeld SCB; Bao Z Ultrahigh electrical conductivity in solution-sheared polymeric transparent films. Proc. Nat. Acad. Sci 2015, 112, 14138–14143. [PubMed: 26515096]

(54). Hulea IN; Fratini S; Xie H; Mulder CL; Iossad NN; Rastelli G; Ciuchi S; Morpurgo AF Tunable Fröhlich polarons in organic single-crystal transistors. Nature Mat. 2006, 5, 982–986.

(55). Podzorov V; Pudalov VM; Gershenson ME Field Effect Transistors on Rubrene Single Crystals with Parylene Gate Insulator. Appl. Phys. Lett 2003, 82, 1739–1741.

(56). Jurchescu OD; Baas J; Palstra TTM Effect of impurities on the mobility of single crystal pentacene. Appl. Phys. Lett 2004, 84, 3061–3063.

(57). Nelson SF; Lin Y-Y Gundlach DJ; Jackson TN Temperature-independent transport in high-mobility pentacene transistors. Appl. Phys. Lett 1998, 72, 1854–1856.

(58). Ji X; Xie H; Zhu C; Zou Y; Mu AU; Al-Hashimi M; Dunbar KR; Fang L Pauli Paramagnetism of Stable Analogues of Pernigraniline Salt Featuring Ladder-Type Constitution. J. Am. Chem. Soc 2020, 142, 641–648. [PubMed: 31829014]

(59). Meyer A; Gleizes A; Girerd JJ; Verdaguer M; Kahn O Crystal structures, magnetic anisotropy properties, and orbital interactions in catena - (μ-nitrito) - bis (ethylenediamine) nickel(II) perchlorate and triiodide. Inorg. Chem 1982, 21, 1729–1739.

(60). Dyson FJ Electron Spin Resonance Absorption in Metals. II. Theory of Electron Diffusion and the Skin Effect. Phys. Rev 1958, 98, 349–359.

(61). Ziatdinov AM; Skrylnik PG Graphite intercalation by nitric acid: conduction ESR and theoretical studies. Chem. Phys 2000, 261, 439–448.

(62). Krinichnyi VI Dynamics of spin charge carriers in polyaniline. Appl. Phys. Rev 2014, 1, 021305.

(63). Bartos P; Anand B; Pietrzak A; Kaszy ski P Functional Planar Blatter Radical through Pschorr-Type Cyclization. Org. Lett 2020, 22, 180–184. [PubMed: 31854992]

(64). Bartos P; Young VG Jr.; Kaszy ski P Ring-Fused 1,4-Dihydro[1,2,4]triazin-4-yls through Photocyclization. Org. Lett 2020, 22, 3835–3840. [PubMed: 32330048]

(65). Perdew JP; Burke K; Ernzerhof M Generalized Gradient Approximation Made Simple. Phys. Rev. Lett 1996, 77, 3865–3868. [PubMed: 10062328]

(66). Becke AD Density-Functional Thermochemistry III. The Role of Exact Exchange. J. Chem. Phys 1998, 98, 5648–5652.

(67). Low JZ; Kladnik G; Patera LL; Sokolov S; Lovat G; Kumarasamy E; Repp J; Campos LM; Cvetko D; Morgante A; Venkataraman L The Environment-Dependent Behavior of the Blatter Radical at the Metal–Molecule Interface. Nano Lett. 2019, 19, 2543–2548. [PubMed: 30884240]

(68). Savu S-A; Biswas I; Sorace L; Mannini M; Rovai D; Caneschi A; Chassé T; Casu MB, Nanoscale Assembly of Paramagnetic Organic Radicals on Au(111) Single Crystals. Chem.-Eur. J 2013, 19, 3445–3450. [PubMed: 23355391]

(69). Junghoefer T; Nowik-Boltyk EM; de Sousa JA; Giangrisostomi E; Ovsyannikov R; Chassé T; Veciana J; Mas-Torrent M; Rovira C; Crivillers N; Casu MB Stability of radical-functionalized gold surfaces by self-assembly and on-surface chemistry. Chem. Sci 2020, 11, 9162–9172. [PubMed: 34123165]

(70). Barth G; Linder R; Bryson C Advances in charge neutralization for XPS measurements of nonconducting materials. Surf. Interface Anal 1988, 11, 307–311.

(71). SADABS v. 2018.1, Bruker AXS, Madison, WI, 2018.

(72). Sheldrick GM SHELXT-Integrated space-group and crystal-structure determination. Acta Cryst. A 2015, 71, 3–8. doi:10.1107/S2053273314026370.

(73). Sheldrick GM Crystal structure refinement with SHELXL. Acta Cryst. C 2015, 71, 3–8. doi:10.1107/S2053229614024218.

(74). Bravais A Etudes Cristallographiques, Gauthier-Villars, Paris, France, 1866, pp 1–290.

(75). Friedel G Etudes sur la loi de Bravais. Bull. Soc. Franc. Mineral 1907, 30, 326–455.

(76). Donnay JDH; Harker D A new law of crystal morphology extending the law of Bravais. Am. Mineral 1937, 22, 446–467.

(77). Macrae CF; Sovago I; Cottrell SJ; Galek PTA; McCabe P; Pidcock E; Platings M; Shields GP; Stevens JS; Towler M; Wood PA Mercury 4.0: from visualization to analysis, design and prediction. J. Appl. Cryst 2020, 53, 226–235. doi: 10.1107/S1600576719014092 [PubMed: 32047413]

(78). Stoll S; Schweiger A EasySpin, a comprehensive software package for spectral simulation and analysis in EPR J. Magn. Reson 2006, 178, 42–55. [PubMed: 16188474]

(79). Rajca A; Mukherjee S; Maren Pink M; Rajca S Exchange Coupling Mediated Through-Bonds and Through-Space in Conformationally-Constrained Polyradical Scaffolds: Calix[4]arene Nitroxide Tetraradicals and Diradical. J. Am. Chem. Soc 2006, 128, 13497–13507. [PubMed: 17031963]

(80). Gennett T; Milner DF; Weaver MJ Role of solvent reorganization dynamics in electron-transfer processes. Theory-experiment comparisons for electrochemical and homogeneous electron exchange involving metallocene redox couples. J. Phys. Chem 1985, 89, 2787–2794.

(81). Giannozzi P; Baroni S; Bonini N; Calandra M; Car R; Cavazzoni C; Ceresoli D; Chiarotti GL; Cococcioni M; Dabo I; Dal Corso A; Fabris S; Fratesi G; de Gironcoli S; Gebauer R; Gerstmann U; Gougoussis C; Kokalj A; Lazzeri M; Martin-Samos L; Marzari N; Mauri F; Mazzarello R; Paolini S; Pasquarello A; Paulatto L; Sbraccia C; Scandolo S; Sclauzero G; Seitsonen AP; Smogunov A; Umari P; Wentzcovitch RM QUANTUM ESPRESSO: a modular and open-source software project for quantum simulations of materials. J. Phys.: Condens. Matter 2009, 21, 395502. [PubMed: 21832390]

(82). Yang CLW; Parr RG Development of the Colle-Salvetti Correlation-Energy Formula into a Functional of the Electron Density. Phys. Rev. B 1988, 88, 785–789.

(83). Grosso G; Parravicini GP Solid State Physics, 1st Ed. San Diego, CA, USA: Academic, 2000, p. 405.

(84). Buongiorno Nardelli M; Cerasoli FT; Costa M; Curtarolo S; De Gennaro R; Fornari M; Liyanage L; Supka AR Wang H PAOFLOW: A utility to construct and operate on *ab initio* Hamiltonians from the projections of electronic wavefunctions on atomic orbital bases, including characterization of topological materials. Comput. Mater. Sci 2018, 143, 462–472.
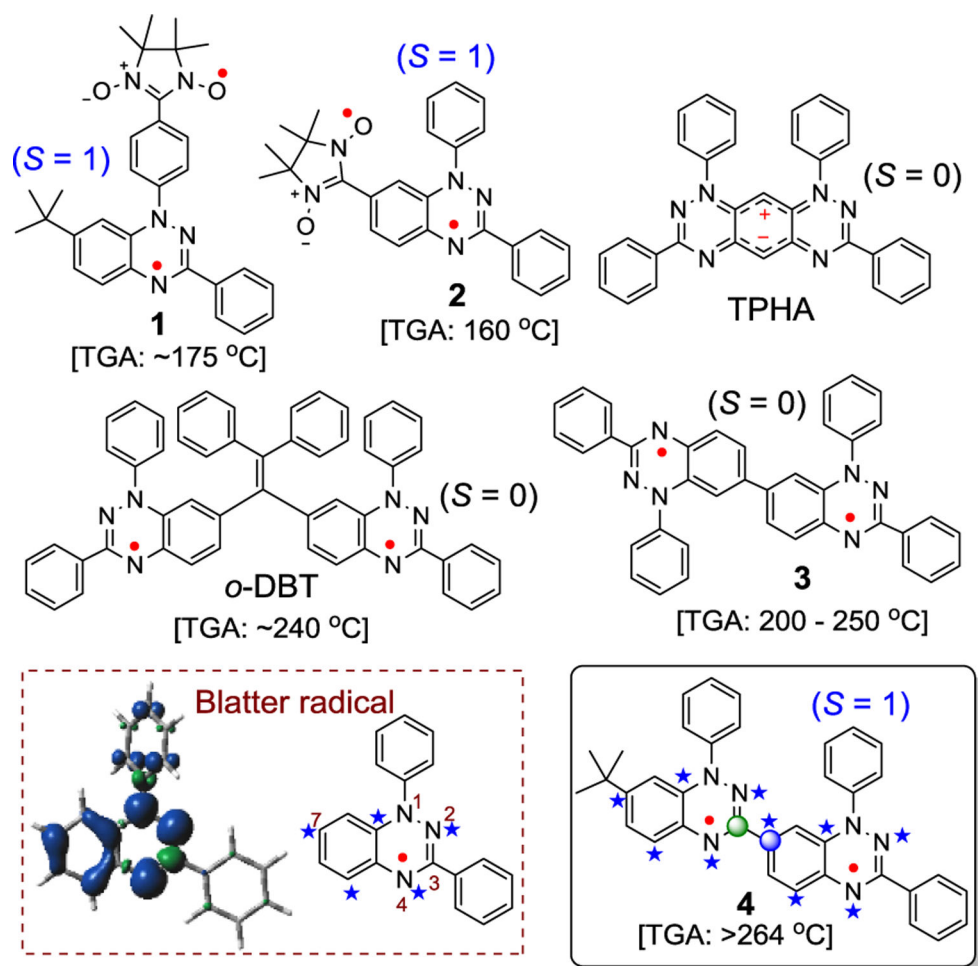
Figure 1.
Blatter-based diradicals: TGA onset of decomposition ≈ 1% mass loss. Blatter radical and its spin density map at the UB3LYP/6–31G(d,p) level of theory; positive (blue) and negative (green) spin densities are shown at the isodensity level of 0.002 electron/Bohr.
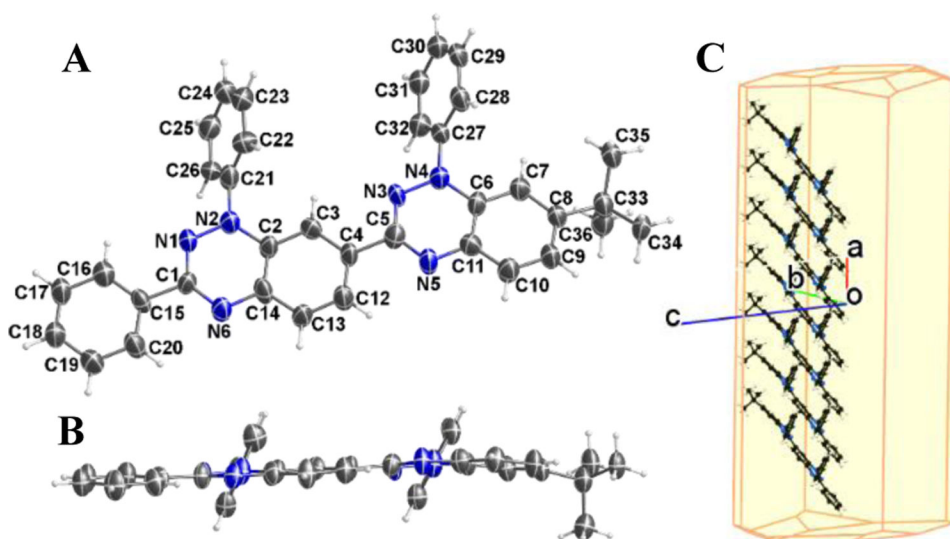
Figure 2.
Single crystal X-ray structure of diradical **4** at 100 K, with carbon and nitrogen atoms depicted using thermal ellipsoids set at the 50% probability level (A and B); the Bravais, Friedel, Donnay and Harker (BFDH) crystal morphoplogy of **4** (C), confirmed with experimental face index; needle and stacking direction are along the *a*-axis. Additional data, e.g., for radical **10**, can be found in the SI: Figs. S1–S6 and Tables S1–S6.
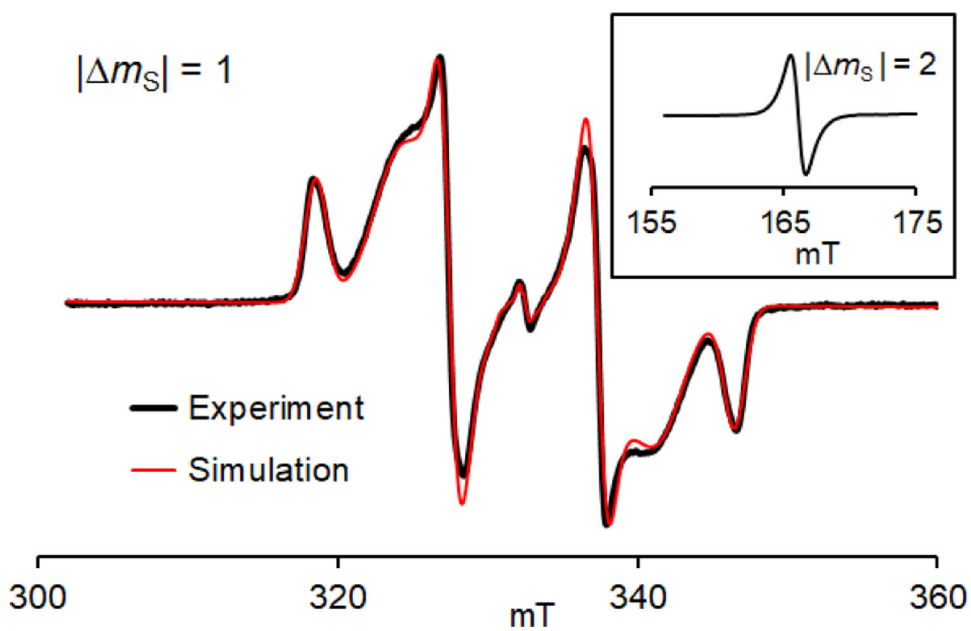
Figure 3.
EPR (110 K, ν = 9.3269 GHz) spectrum for 0.54 mM diradical **4** in toluene/chloroform, 3:1 glass; a small center peak corresponds to monoradical impurity (ca. 5%). Inset: the $|m_s| = 2$ transition. Spectral simulation of the $|m_s| = 1$ region (rmsd = 0.0197, see: Table 1 and Figs. S18–S20, SI.
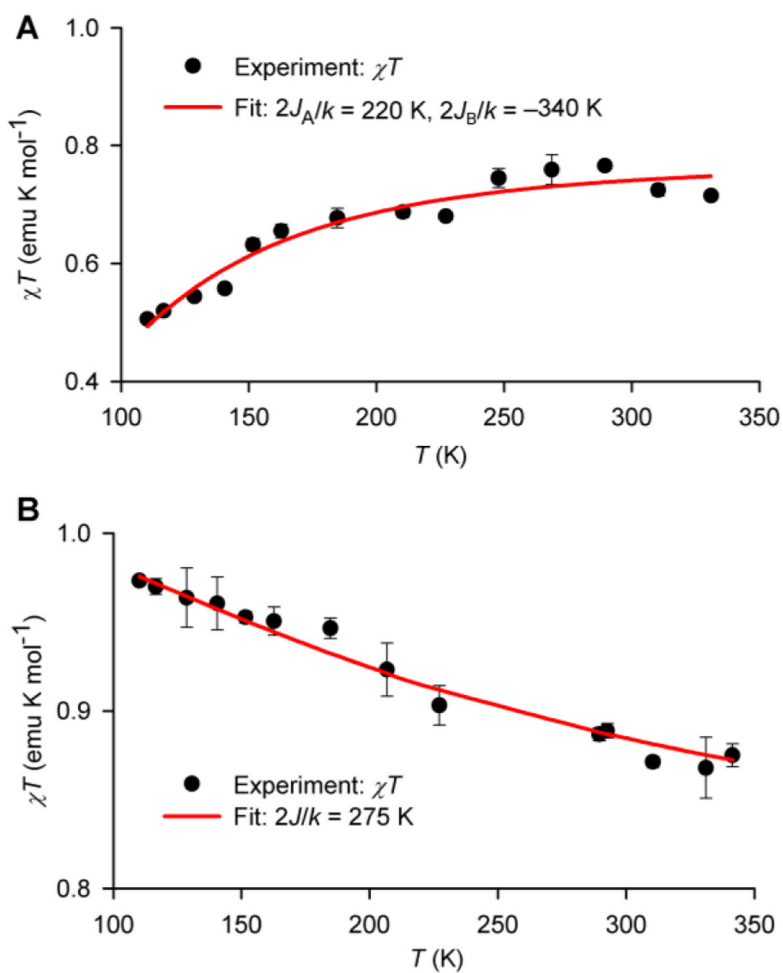
Figure 4.
EPR spectroscopy of diradical **4**: plots and numerical fits of χT vs T in toluene/chloroform (4:1) (**A**) and polystyrene (**B**). Further details are reported in the SI: Table S7, Figs. S16, S21–S23, Eqs. S1 and S2.
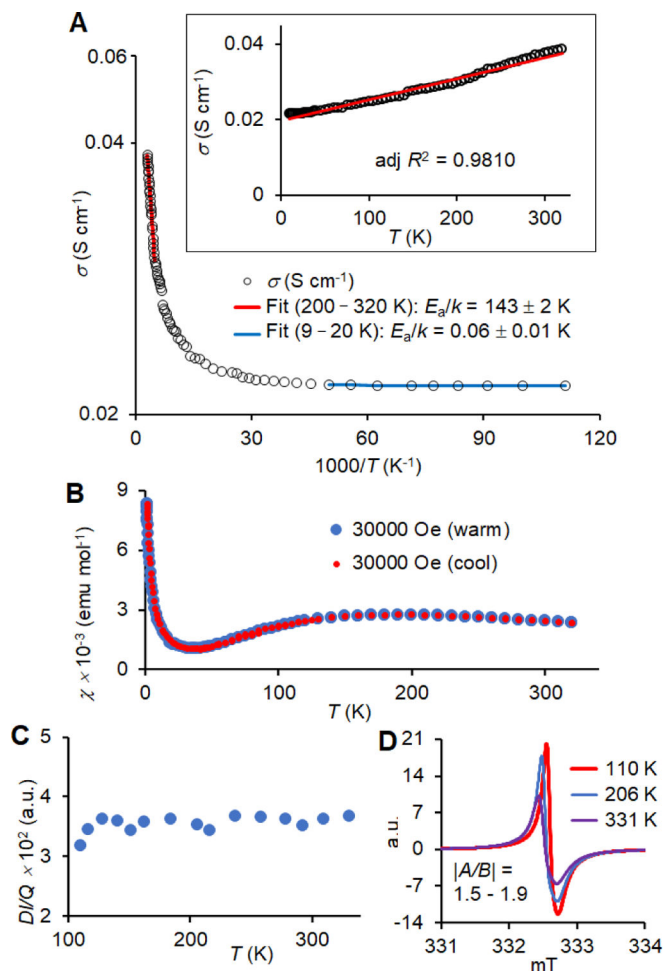
Figure 5.

Solid state characterization of diradical **4**. **A**, <u>main plot</u>: single crystal conductivity, σ, of diradical **4** (plotted on a logarithmic scale) as a function of the reciprocal temperature ($1000/T$), with the fits in the high- and low-temperature ranges, showing effective activation energies (E_a/k). <u>Inset plot</u>: single crystal σ vs T, showing near-linear relationship. **B**, SQUID magnetometry of polycrystalline **4**: magnetic susceptibility, χ vs T for $T = 1.8 - 320$ K. **C** and **D**, EPR spectroscopy of polycrystalline **4** with particle size of <75 μm: $DI/Q \sim \chi$ vs T and representative EPR spectra, showing Dysonian line-shape, where DI is a double integrated intensity and Q is a microwave cavity quality factor. Further details are reported in the SI: Tables S8 and S9, Figs. S12, S13, S15, S17, S24–S40.
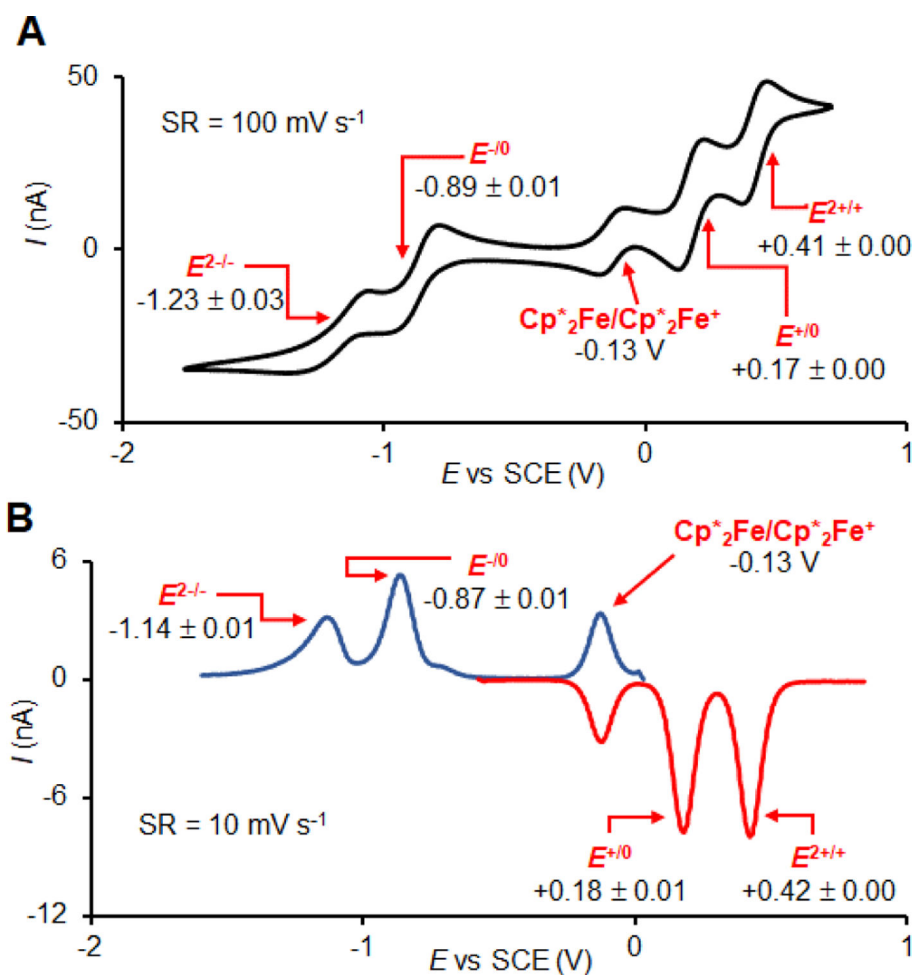
Figure 6.
Cyclic voltammetry (CV, **A**) and differential pulse voltammetry (DPV, **B**) of diradical **4** in 0.1 M tetrabutylammonium hexafluorophosphate in dichloromethane. Scan rates (SR) are 100 and 10 mV s^{-1}. Redox potentials are given as mean ± stddev with n = 7–8 (CV) and n = 4 (DPV). For further details, including square wave voltammetry, see: SI.
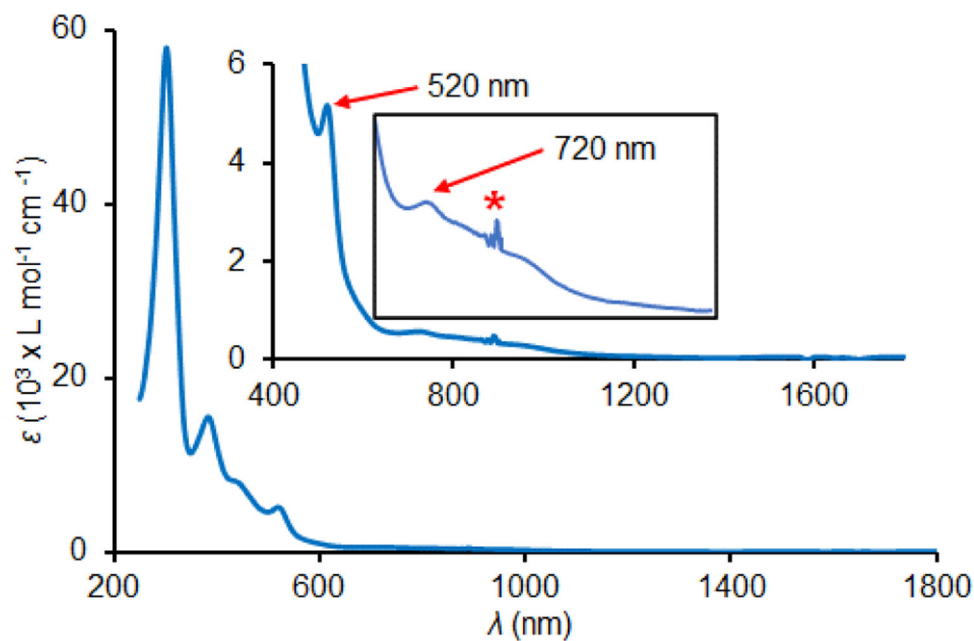
Figure 7.
UV–vis–NIR (294 K) absorption spectrum for 0.2 mM diradical **4**. Bands at λ_{max} = 303, 384, 520, and 720 nm have the following extinction coefficients: ε_{303} = 6.0 × 10^4 L mol^{-1} cm^{-1}, ε_{384} = 1.6 × 10^4 L mol^{-1} cm^{-1}, ε_{520} = 5.3 × 10^3 L mol^{-1} cm^{-1}, and ε_{720} = 5.8 × 10^2 L mol^{-1} cm^{-1}. Feature at $\lambda \approx$ 900 nm, marked with a red asterisk is an instrumental artefact (change of grating).
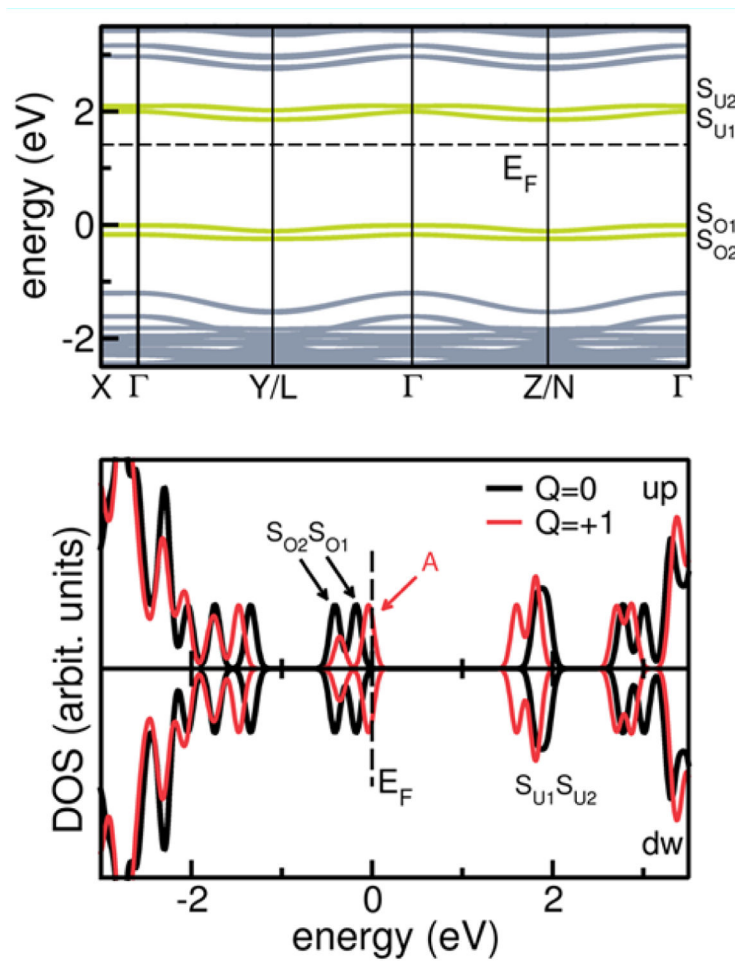
Figure 8.
Crystalline diradical **4** at the B3LYP level of theory. Fermi energy (E_F) level is indicated with dashed lines. <u>Top:</u> Band structure. Single occupied (S_{O1}, S_{O2}) and single unoccupied (S_{U1}, S_{U2}) bands are marked in green. <u>Bottom:</u> Spin-resolved density-of-states (DOS), for neutral ($Q = 0$, black line) and charged ($Q = +1$, red line) crystals. Peak A identifies the defect level in the charged system.
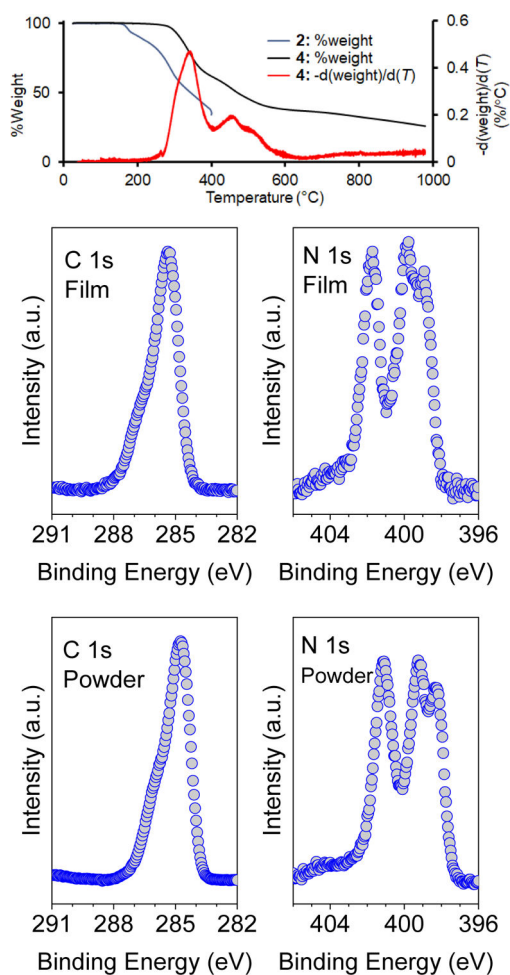
Figure 9.

<u>Top:</u> Thermogravimetric analysis with IR spectra of diradicals **2** and **4** under N_2; heating rate = 5 °C min^{-1}. For further details, including IR spectra, see: SI, Figs. S41 and S42. <u>Bottom:</u> C 1s and N 1s core level spectra of a multilayer of **4** deposited on SiO_2/Si(111) substrate, compared to the powder spectra.
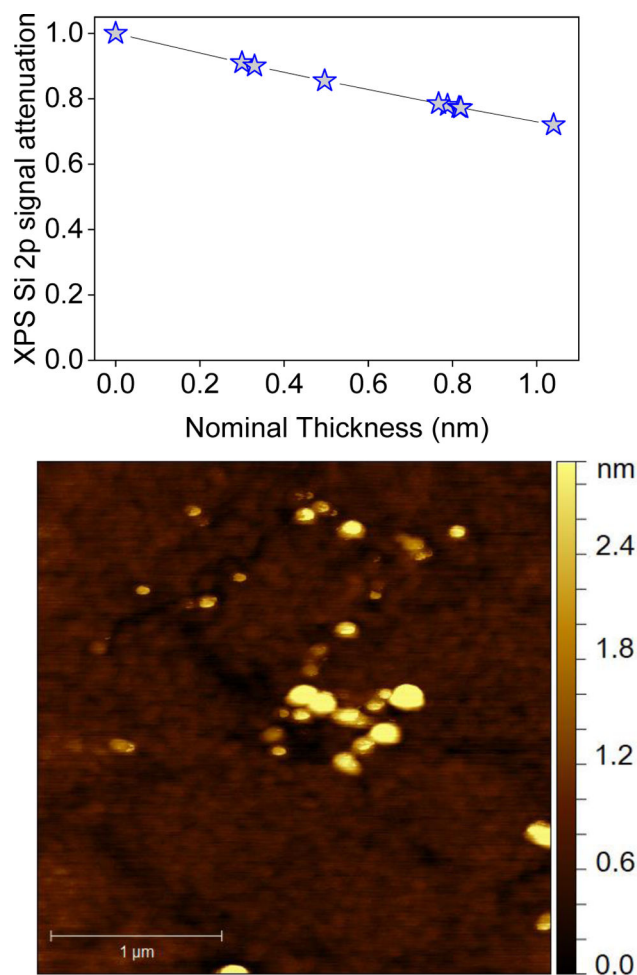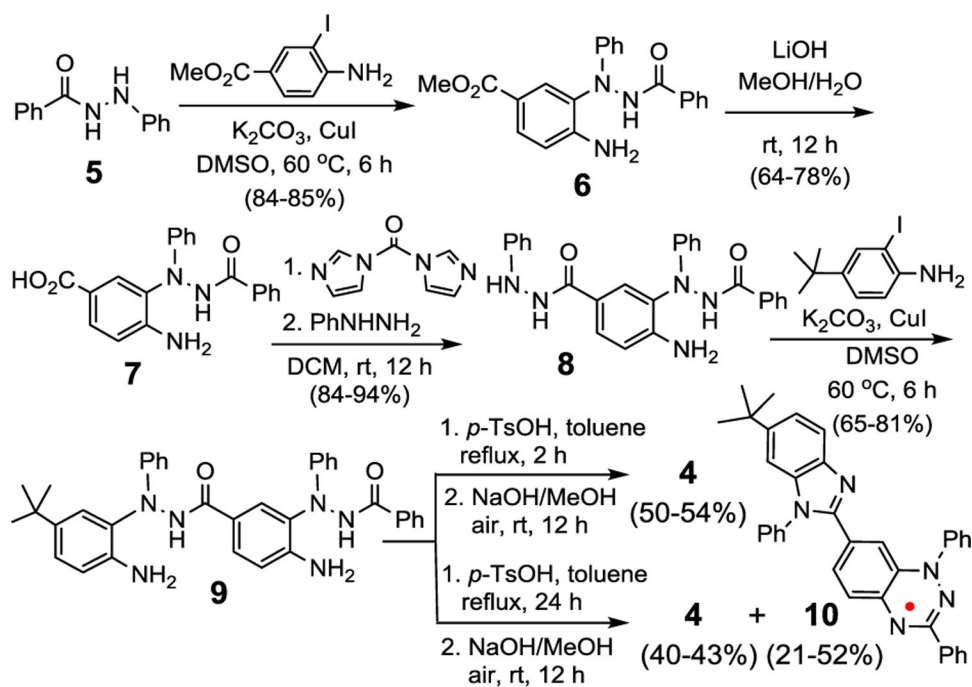
Figure 10.
<u>Top:</u> Attenuation of the Si 2p XPS signal, normalized to the corresponding saturation signal at zero film thickness as a function of the film nominal thickness, deposition at room temperature. The line is a guide to the eye. <u>Bottom:</u> A typical 3 μm × 3 μm AFM image.

Scheme 1.
Synthesis of diradical **4** and monoradical **10**.

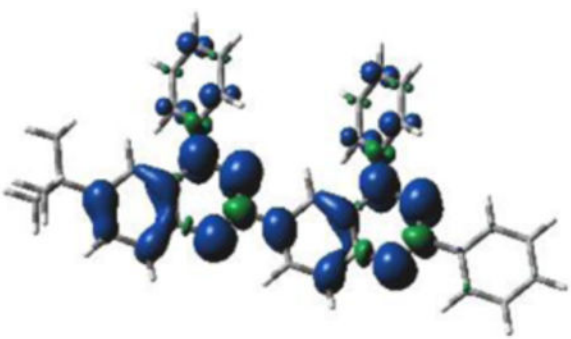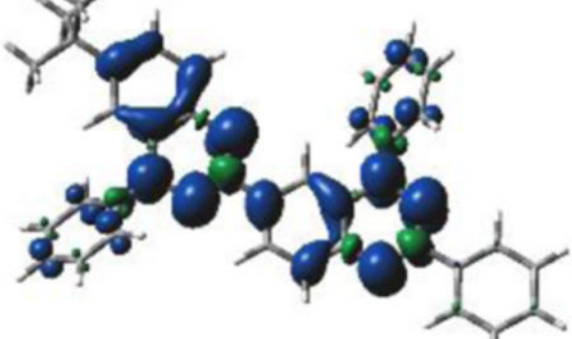**Table 1.**

EPR parameters for triplet states of diradicals.

Diradicals	D (MHz)	E (MHz)	g_x	g_y	g_z	g_{iso}[a]
1	69.6	4.2	2.0069	2.0010	2.0052	2.0044
2	242	35.1	2.0072	2.0026	2.0052	2.0050
3	ca. 75	na	na	na	na	na
o-DBT	126	39	na	na	na	na
4	391	35.9	2.0042	2.0027	2.0041	2.0037
4A[b]	406	71	2.0043	2.0023	2.0041	2.0036
4B[b]	410	60	2.0042	2.0022	2.0042	2.0036

[a]$g_{iso} \approx (g_x + g_y + g_z)/3$.

[b]Computed with ORCA (Table S13, SI).

Table 2.

DFT computations: conformers 4A and 4B of diradical 4.

4A[a]

4B[a]

Medium	Conformer	State	E_T[b]	$<S^2>$	E_{ST}[c]
Gas ph.	4A	Triplet	0.00	2.0363	0.00
		BSsinglet	-	1.0283	1.37
	4B	Triplet	0.05	2.0359	0.00
		BSsinglet	-	1.0014	0.34
THF	4A	Triplet	0.00	2.0339	0.00
		BSsinglet	-	1.0271	1.22
	4B	Triplet	0.14	2.0338	0.00
		BSsinglet	-	0.9993	0.22

[a] Spin density plots for triplet states of **4**A and **4**B.

[b] E_T (kcal mol^{-1}) relative energies for triplet states.

[c] E_{ST} (kcal mol^{-1}) is computed using eq. S4, SI.